On probabilistic aspects in the dynamic degradation of ductile materials

Hervé Trumel, François Hild, Gilles Roy, Yves-Patrick Pellegrini, Christophe Denoual

HAL Id: hal-00410324
https://hal.archives-ouvertes.fr/hal-00410324

On probabilistic aspects in the dynamic degradation of ductile materials

Hervé Trumel [a] [1], François Hild [b], Gilles Roy [c],
Yves-Patrick Pellegrini [d], Christophe Denoual [d]

[a]*CEA, DAM, Le Ripault, F-37260 Monts, France.*

[b]*LMT-Cachan, ENS Cachan / CNRS / UPMC / PRES UniverSud Paris*
61 avenue du Président Wilson, F-94235 Cachan Cedex, France.

[c]*CEA, DAM, Valduc, F-21120 Is-sur-Tille, France.*

[d]*CEA, DAM, F-91272 Arpajon, France.*

Abstract

Dynamic loadings produce high stress waves leading to the spallation of ductile materials such as aluminum, copper, magnesium or tantalum. The main mechanism used herein to explain the change of the number of cavities with the stress rate is nucleation inhibition, induced by the growth of already nucleated cavities. The dependence of the spall strength and critical time with the loading rate is investigated in the framework of a probabilistic model. The present approach, which explains previous experimental findings on the strain-rate dependence of the spall strength, is applied to analyze experimental data on tantalum.

Key words: A Dynamic ductile damage, B Probabilistic model, C Tantalum

1 Introduction

The impact of a projectile on a target generates two shock waves propagating in opposite directions. Meeting free surfaces, these shock waves reflect back as two release waves, which generally meet together at a definite location, the spall plane.

---

[1] Formerly at LMPM, ENSMA (UMR CNRS 6617), Téléport 2, BP 40109, 1 avenue Clément Ader, F-86961 Futuroscope Chasseneuil Cedex. Corresponding author.
  Email addresses: `herve.trumel@cea.fr` (Hervé Trumel),
`hild@lmt.ens-cachan.fr` (François Hild), `gilles.roy@cea.fr` (Gilles Roy),
`yves-patrick.pellegrini@cea.fr` (Yves-Patrick Pellegrini),
`christophe.denoual@cea.fr` (Christophe Denoual).

Their superposition produces a triaxial tensile ramp loading that often results, prior to fracture, in the nucleation, growth, and coalescence of microvoids in most metals. This phenomenon is known as "ductile spalling."

Although discovered long ago and studied by many authors (see Meyers and Aimone, 1983; Curran et al. 1987; Grady, 1988 for reviews), its modeling still raises open questions. Since the pioneering works of Carroll and Holt (1972) and of Glennie (1972), void growth has by far been the main concern. This led many authors to derive elastic-viscoplastic-damage models using the overall porosity as damage variable (see, *e.g.,* Eftis and Nemes, 1991; Cortes 1992), often comparable to the quasi-static class of Gurson-like models (Gurson, 1977; Tvergaard, 1999). In these models, nucleation and coalescence are generally dealt with in an empirical fashion. In the recent years, however, renewed attention has been paid to these processes. The present paper aims at addressing the question of nucleation, coalescence being put aside for future work (the interested reader may refer to some recent works on this topic by Thomason (1999), Tonks et al. (2002), Bontaz-Carion et al. (2006)).

Some recent interrogations in relation to the definition of a dynamic representative volume element (Roy, 2003; Dragon and Trumel, 2003) seem to indicate that the overall porosity is not a sufficient parameter, and that the entire size distribution should be accounted for. The long neglected question of micro-inertia is the subject of a continued effort (Ortiz and Molinari, 1992; Tong and Ravichandran, 1995; Wang and Jiang, 1997; Molinari and Mercier, 2001; Wu at al., 2003; Roy, 2003). Not only does it slow down the growth of individual voids, but also does it confine each void within an evolving neighborhood bounded by an elastic relaxation wave. Hence, dynamic void interactions are strongly linked to inter-void spacing, itself driven by the nucleation process. The latter thus appears as a crucial mechanism. This is all the more the case that Roy (2003), studying pure tantalum over a large range of shock levels and durations, showed extreme size distributions to be present in recovered samples, indicating that nucleation is a continuous process taking place up to coalescence. Figure 1 shows a tantalum sample recovered after an impact at 270 m/s by a coffer flyer plate (Roy, 2003), and containing isolated voids up to about 100 μm in diameter (Even larger voids can be observed at lower impact velocities). A detailed account of the nucleation process is clearly beyond the present state of knowledge, although much progress is being made using atomistic tools (see in particular Rudd and Belak, 2002). However, the probabilistic approach is an interesting alternative, as shown by Grady and Kipp (1979; 1980), Denoual and Hild (2000) for dynamic fragmentation of brittle materials, and more recently by Molinari and Wright (2005), Czarnota et al. (2006, 2008) for ductile spalling. In both cases, the purely deterministic description of void growth is combined with a stress-dependent probability of void nucleation, in the form of a Weibull-like model. Czarnota et al. (2006, 2008) define a probability of nucleating new voids; in addition, Denoual and Hild (2000) use a spatial distribution of crack nuclei among which new cracks are activated. Void interactions are also treated in a different fashion. Czarnota et al. (2006, 2008) use the overall porosity to describe the weak-
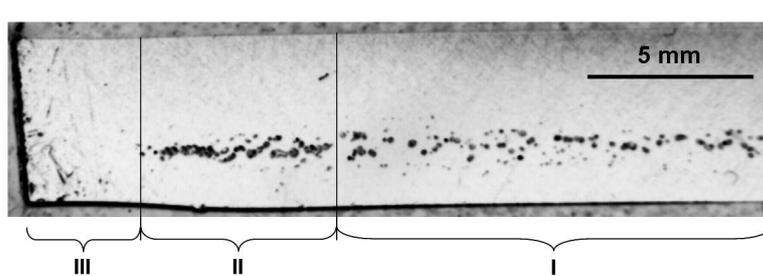
2

Fig. 1. Example of a 5 mm thick tantalum sample damaged by a symmetric impact at 270 m/s by a CuC2 flyer plate (the shock wave traveled from top to bottom); zone I: uniaxially loaded, zone II: biaxially loaded, zone III: rapidly unloaded. Only the left half of the target is shown. The right edge is close to the symmetry axis.

ening effect of already present voids, whereas Denoual and Hild (2000) consider microcrack growth as a spatially bounded relaxation process which inhibits nucleation in relaxed zones. In this respect, the degree of coupling is stronger in the last approach.

It is intended here to assess the relevance of inhibition concepts for fragmentation (Mott, 1947; Grady and Kipp, 1980; Denoual and Hild, 2000) to analyze ductile spalling processes. Rather than precisely describing joint nucleation, growth processes and their couplings, this paper aims at setting the fundamentals of the theory to demonstrate its potentialities within the simplest possible theoretical framework. Section 2 shows how the deterministic and probabilistic parts of the model are interlinked, and puts the emphasis on inertial growth, which drives the inhibition process. Section 2.3.2 presents an application to ramp loading, generally agreed to be representative of the real loading in the spall plane in the lack of any phase transition process, and ends up with a closed-form solution of the whole problem. A very simple overall damage model is proposed in Section 3.1, and yields an analytical expression for the spall stress, *i.e.,* the maximum tensile stress the material can sustain during the whole spalling process. Through a thorough examination of the experimental data of Roy (2003), Nicollet et al. (2001), and Bontaz-Carion et al. (2006) on pure tantalum, the model is identified and discussed in Section 4, and applied tentatively to other materials in Section 5.

2 Nucleation and growth in ductile materials

2.1 Model outline

As introduced above, the physical process of nucleation and growth during early stages of ductile spallation is complex. Wave propagation induces transient macroscopic stress fields. At a finer (mesoscopic) spatial scale, local fields experience fluctuations due to the polycrystalline nature of the materials considered (Fig. 2(a)).
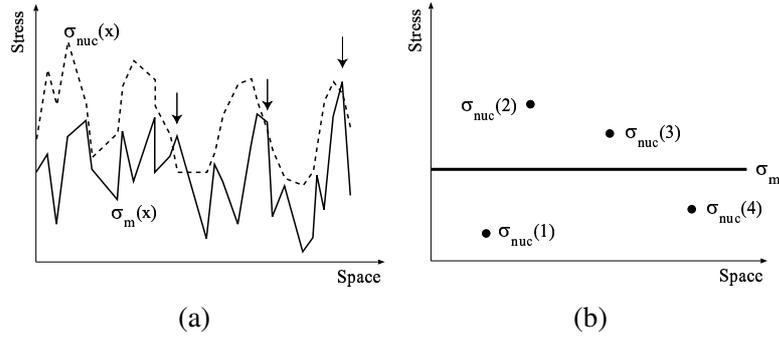
3

Fig. 2. Simplifying assumptions of the nucleation model (nucleation conditions met at arrows). a) Physical situation: applied tensile stress σ_m and nucleation level σ_{nuc} as continuous random fields. b) Simplification: uniform applied stress, and field of nucleation thresholds split up into discrete sites of random locations and threshold values.

When the local hydrostatic stress $\sigma_m(\mathbf{x}, t)$ exceeds some local nucleation threshold $\sigma_{nuc}(\mathbf{x})$, cavities are nucleated and start to grow.

As shown by Roy and Villechaise (Roy, 2003), in pure tantalum nucleation sites are primarily located at grain boundaries, especially triple points [2]. Growing cavities in turn induce relaxation zones in which local stresses decrease, thus decreasing the probability of nucleating voids in these zones, and out of which local stresses remain unaltered. Hence, any volume element in which macroscopic stresses are uniform prior to nucleation evolves into a volume containing growing perturbed zones in an otherwise unperturbed uniformly loaded matrix.

According to Roy (2003), isolated voids remain spherical from very small to very large sizes, implying that local fluctuations of material behaviour do not seem to influence void growth. Hence, a first simplification will consist in neglecting the effects of the polycrystalline nature of the material of the matrix, and therefore on macroscopic stresses. We thus assume *uniform loading*, in a pristine matrix material which contains a *random spatial distribution of void nuclei* at which the elastic-plastic properties of matrix material *strongly fluctuate* around their bulk value (Fig. 2(b)). Furthermore, the matrix is assumed perfectly plastic hereafter. Neglecting temperature, viscosity and strain hardening is performed for the sake of simplicity, and can be relaxed in more detailed (future) analyses. During further evolutions, activated voids are the only local heterogeneities that will affect macroscopic stresses. In this context, a voided volume is viewed as a matrix loaded by a uniform hydrostatic tensile stress σ_m, containing several (possibly overlapping) perturbed zones.

Second, the joint effects of local stress fluctuations and of local weaknesses are accounted for through a *stress-dependent nucleation probability*. It will be fur-

---

[2] This picture is valid when the material is pure. When second-phase particles or precipitates are present, so-called heterogeneous nucleation processes take place. The present paper focuses on the first mechanism.

4

ther assumed that the inhibition phenomenon is total in strongly relaxed zones. Hence, matrix stresses will be considered as the only driving force for nucleation and growth.

Third, given the high level of triaxiality, as well as the spherical shape of the voids observed by Roy (2003), macroscopic shear stresses will be neglected, such that $\sigma_{ij} = \sigma_{\mathrm{m}}\delta_{ij}$. From now on, σ_{m} will simply be referred to as "the stress."

Growth drives the extension of relaxation zones, and thus the inhibition process. The growth model must therefore be carefully chosen. On the one hand, as stressed by Ortiz and Molinari (1992), Wang and Jiang (1997), Roy (2003), Dragon and Trumel (2003), Molinari and Wright (2005), Czarnota et al. (2006), inertial effects are overwhelmingly important. On the other hand, elasticity should not be neglected, since it has a strong effect on early growth (Denoual and Diani, 2001; Roy, 2003). Advantage will be taken here of a simplified approach proposed by Roy (2003), from the work of Forrestal and Luk (1998). This approach shows that growth cannot take place if the macroscopic stress is less than a *cavitation* threshold, as shown by many authors in the quasi-static case (Mandel, 1966; Hou and Abeyaratne, 1992; Denoual and Diani, 2001).

We now proceed to assemble the above-listed ingredients. In a pristine examination volume V subjected to uniform stress $\sigma_{\mathrm{m}}(t)$, we assume the number N of *active* nucleation sites, of associated random nucleation stress $\sigma_{\mathrm{nuc}}(\mathbf{x})$ where $\mathbf{x}$ is the site location, to follow a Point-Poisson distribution of intensity n_{tot} (the average volume density of active sites). The probability of finding N active sites in V is

$$P(N, V) = \frac{(n_{\mathrm{tot}}V)^N}{N!} \exp\left(-n_{\mathrm{tot}}V\right). \tag{1}$$

In the above definition, a nucleation site at location $\mathbf{x}$ is said *active* at t (*i.e.,* can potentially initiate a void) if $\sigma_{\mathrm{m}}(\tau) \geq \sigma_{\mathrm{nuc}}(\mathbf{x})$ for any past time $0 \leq \tau \leq t$. It will effectively give birth to a void only if not inhibited (effects of inhibition are dealt with in Sec. 2.3.1). Introduce then $\sigma_{\max}(t) = \max_{0 \leq \tau \leq t} \sigma_{\mathrm{m}}(\tau)$, the maximum hydrostatic stress reached up to time t. According to experimental findings (Roy, 2003), the density of nucleated cavities is stress-dependent. This prompts us to further write $P(N, V)$ in the form of the so-called Weibull-Poisson law by taking (Gulino and Phoenix, 1992; Jeulin, 1991; Denoual and Hild, 2002)

$$n_{\mathrm{tot}}(t) = n_0 \left[\frac{\langle \sigma_{\max}(t) \rangle}{\sigma_0}\right]^m, \tag{2}$$

where m is the Weibull modulus which characterizes the *scatter* in nucleation levels (weak scatter corresponds to a high m value, and conversely), σ_0 is a scale parameter relative to a reference density n_0, and $\langle \star \rangle$ are Macauley brackets that denote the positive part of $\star$. In Eqn. (1), the product $n_{\mathrm{tot}}V$ thus represents the average number of sites in V where σ_{m} has overcome the nucleation threshold. Equation (2) indicates that the higher $\sigma_{\max}(t)$, the more nucleation sites are active. It should be noted

that a classical Weibull expression is retrieved within the weakest link framework, see Appendix A.

Since Eqs. (1) and (2) describe the probability of activating N sites in a pristine uniformly loaded volume V, they also hold (with V replaced by V') in the *uniformly loaded part V'* of a larger *voided* volume, by definition of σ_{m}, and by the above assumption of total inhibition. The volume V' is found by subtracting from V the volume of inhibited zones, thus accounting for possible overlaps between individual inhibition zones that grow out of each activated site. Since inhibition is related to stress relaxation, V' depends on the growth model, which is addressed now.
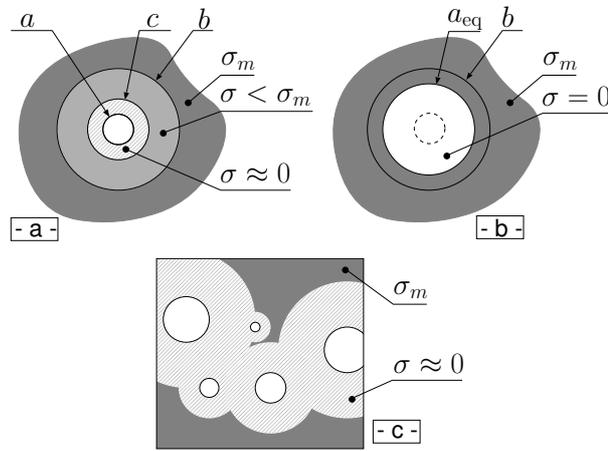
2.2 A simplified growth model

Fig. 3. Equivalent hollow sphere model. a– Real elasto-plastic hollow sphere. b– Simplified representation of equivalent elastic energy. c– Schematic representation of overlapping relaxed zones. See Sec. 3.1 for a discussion of Figs. (b) and (c).

Cavity nucleation can be understood as a bifurcation process in the sense of Hou and Abeyaratne (1992). Once nucleated, any new cavity starts to grow. As shown for example by Hopkins (1960), Hunter and Crozier (1968), Glennie (1972), or Roy (2003), an isolated growing cavity of radius $a(t)$ can be seen as an expanding volume bounded by an elastic relaxation wave at radius $b(t)$. This volume consists in an outer elastic zone, and an inner elastic-plastic region, separated by an evolving elastic-plastic boundary of ("plastic") radius $c(t)$ (Fig. 3a). Both regions are referred to as "the matrix" hereafter. Denoual and Diani (2001), Tonks et al. (2002) showed that the early growth can be decomposed into three distinct phases. The first one is essentially elastic, until the hydrostatic stress reaches a "cavitation threshold" (see below). There, bulk elastic energy release induces a violent elastic-plastic expansion of the cavity, until the third phase of stationary expansion is established.

Strong relaxation occurs inside the elastic-plastic zone. This is illustrated numeri-
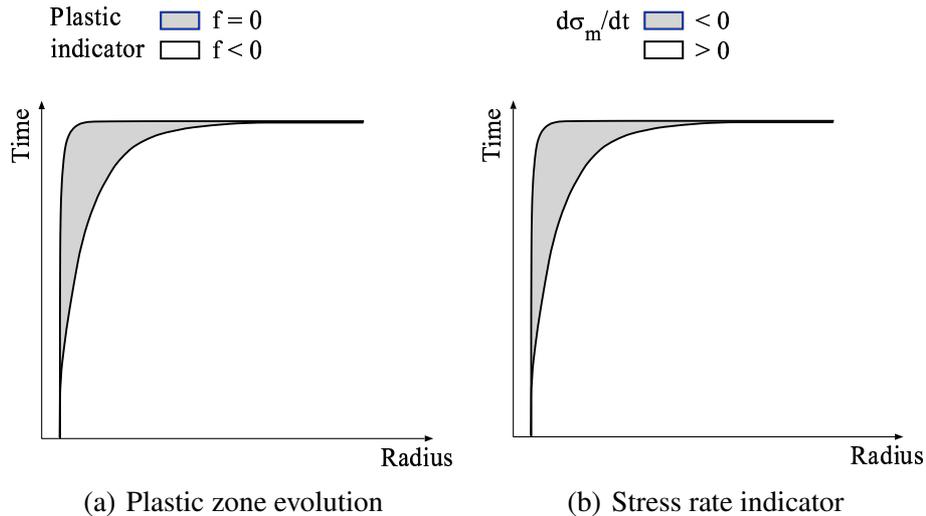
(a) Plastic zone evolution   (b) Stress rate indicator

Fig. 4. Space-time diagram for a hollow sphere (initial outer radius: $b = 12.5$ μm, initial inner radius $a = 0.58$ μm) submitted to a stress rate of 2 GPa/μs on the outer radius. The material parameters are those of tantalum (Table 1). The plastic zone coincides with the region in which the local pressure decreases, in spite of an overall pressure increase.

cally, by submitting a hollow tantalum sphere of initial outer and inner radii of 12.5 and 0.58 μm respectively (*i.e.,* an initial porosity of 10^{-4}) to a hydrostatic stress ramp of 2 GPa.μs^{-1} applied on the outer boundary. Figure 4 shows the space-time domain where the matrix is yielding (Fig. 4(a)), and that of varying σ_m (Fig. 4(b)). It is seen that σ_m decreases inside the plastic zone although the applied stress keeps increasing. Plastic zones can thus be seen as (and identified to) *inhibition zones* for further void nucleation, and this is exploited in the next section. This shows that unlike previous works (Wu et al. 2003; Molinari and Wright, 2005; Czarnota et al. 2006), it is not sufficient to establish a link between the macroscopic stress and the cavity radius a, namely, the link between these quantities and c must be known as well.

Roy et al. (2002, 2003) checked numerically that the cavitation stress is independent of the macroscopic strain-rate, and that the transient regime is brief. Accordingly, and since this allows for closed-form solutions, a purely stationary model is used here, with $a(t) = \dot{a}\,t$, $c(t) = \dot{c}\,t$, where $\dot{a}$ and $\dot{c}$ are constant growth velocities. The approach used (detailed in Appendix B) is adapted from the work of Forrestal and Luk (1988), itself derived from earlier works dealing with isolated cavity growth under internal hydrostatic stress (Hopkins, 1960; Hunter and Crozier, 1968).

Thus, for an isolated cavity in an infinite medium subjected to a remote tensile stress $\sigma_m(t)$, an implicit equation links $\dot{c}$ and $\sigma_m(t)$ to $\dot{a}$ [Eqs. (B.14) and (B.15)]. A first-order expansion valid in the low stress rate regime (assuming $\dot{c} \ll c_P$ *and* $\dot{a} \ll c_P$, where $c_P = \sqrt{K/\rho_0}$ is the so-called plastic velocity (Zeldovich and Raizer, 2002), K is the bulk modulus, and ρ_0 is the reference density), then provides the

7

additional proportionality relationship

$$\dot{c} = \beta^{-1/3}\,\dot{a}, \tag{3}$$

where β is defined by Eqn. (B.16) in terms of K, μ the shear modulus, and Y the yield stress. For most materials $\beta \ll 1$. In turn, a similar first-order expansion provides relationship (B.18), namely,

$$\dot{a} = \dot{a}_0 \langle \sigma_{\mathrm{m}}/\sigma_{\mathrm{cav}} - 1 \rangle^{1/2} \tag{4}$$

between the void growth velocity and the applied tensile stress, where σ_{cav} is the cavitation threshold, and where $\dot{a}_0$ is a characteristic void growth velocity in the material. Both quantities depend only on K, μ and Y, with $\dot{a}_0$ depending on ρ_0 as well (see Appendix B for explicit expressions of these quantities). Combining Eqs. (3), (4) yields

$$\dot{c} = k\,c_P\,\langle \sigma_{\mathrm{m}}/\sigma_{\mathrm{cav}} - 1 \rangle^{1/2} \tag{5}$$

where $k \equiv \beta^{-1/3}\dot{a}_0/c_P$ is a numerical coefficient ($k\,c_P$ being a characteristic growth velocity of the plastic region). For Al, Cu and Ta, k varies between 0.3 and 0.5.

Equation (5) constitutes a particular instance of the more general class of threshold-like expressions

$$\dot{c} = k\,c_P\langle \sigma_{\mathrm{m}}/\sigma_{\mathrm{cav}} - 1 \rangle^{\alpha}, \tag{6}$$

where $\alpha \geq 0$ is a stress-sensitivity exponent, and where the nucleation stress σ_{nuc} of Fig. 2 is identified to the cavitation threshold σ_{cav}. No significant growth of the microvoid population should occur unless cavitation conditions are met. This general expression covers the present case, as well as the "quasi-brittle" case for which $\alpha = 0$ (Denoual et al. 1997). In the case of monotonically increasing loading $\sigma_{\mathrm{m}}(t)$, upon integrating (6) over time we obtain $c(t)$ in the form

$$c(t) = C(t - t_{\mathrm{nuc}}), \qquad (t > t_{\mathrm{nuc}}) \tag{7}$$

where C is some function and where t_{nuc} is the nucleation time obtained as a solution to

$$\sigma_{\mathrm{m}}(t_{\mathrm{nuc}}) = \sigma_{\mathrm{cav}}. \tag{8}$$

2.3 Elementary cell assembly

2.3.1 Dynamic inhibition model

So far, we described the behavior of *isolated* cavities only, in a deterministic way. The *collective* behavior of the population of voids is now considered. Henceforth, overlined quantities are used for macroscopic variables that represent statistical (or more phenomenological) averages of their microscopic counterparts.

8

The intrinsic probabilistic nature of the nucleation and growth process should be embodied in some random variability of the local elastic and plastic properties of the material Y, μ, K and ρ_0. Equation (8) shows that under some prescribed time-dependent loading, a random set $\{\sigma_{\text{cav}}\}$ of cavitation or generic nucleation thresholds (see Fig. 2) can be mapped to a random set $\{t_{\text{nuc}}\}$ of nucleation times. Randomness in the process is thus introduced through the following crucial bold assumption that emphasizes the part played by nucleation times: in Eqn. (7) the nucleation time t_{nuc}, which physically depends on the above material parameters *and* on the local loading, will be considered as a random variable, whereas material parameters, and parameters which define the field loading function, will be considered as "averaged" ones whenever they enter the definition of the function C itself.

Section 2.2 substantiates the identification between plastic regions and zones of total nucleation inhibition. Accordingly, the inhibition volume V_{inh} associated to an *isolated* cavity is taken hereafter proportional to the plastic radius c

$$V_{\text{inh}} = V_{\text{inh}}(t - t_{\text{nuc}}) = S\,c^3, \tag{9}$$

where S is a shape parameter, and the functional time dependence of V_{inh} stems from Eqn. (7).
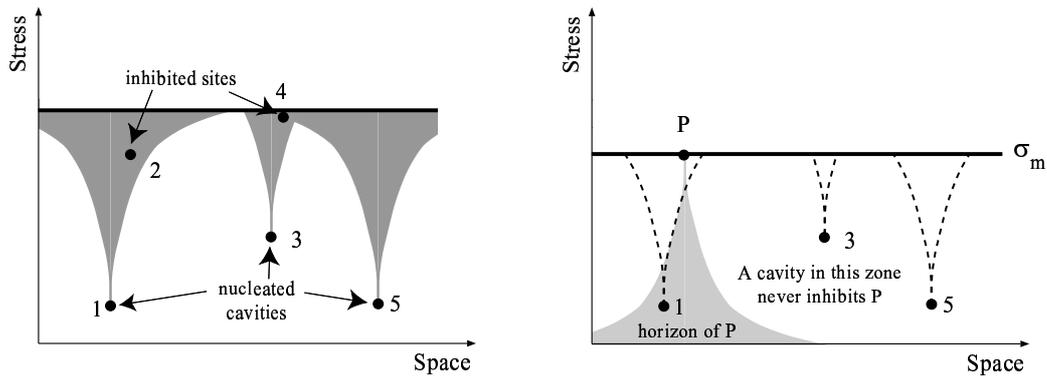
(a) Inhibition phenomena. In grey are relaxed zones where void nucleation is inhibited.

(b) Horizon of a site P. Any active site in the grey zone inhibits further cavity nucleation at P.

Fig. 5. Inhibition and horizon concepts.

New voids will nucleate from active nucleation sites (in the sense of Sec. 2.1) only if they do not belong to *any* relaxed zone produced by previously nucleated growing voids, as depicted in Fig. 5(a). Thus n_{nuc}, the volume density of centers of nucleated voids, is related to n_{tot} defined in Eqn. (2) by

$$\frac{\mathrm{d}n_{\text{nuc}}}{\mathrm{d}t} = (1 - P_{\text{inh}})\frac{\mathrm{d}n_{\text{tot}}}{\mathrm{d}t}, \tag{10}$$

with $n_{\text{nuc}}(0) = n_{\text{tot}}(0) = 0$. This equation, which implements inhibition effects

in the model, involves the inhibition probability (identified with an overall volume fraction of inhibited regions)

$$P_{\text{inh}}(t) = 1 - \exp\left[-\overline{V}_{\text{inh}}(t)n_{\text{tot}}\left\{\sigma_{\text{m}}(t)\right\}\right], \qquad (11)$$

where $\overline{V}_{\text{inh}}$, the *mean* volume of the inhibition zone, is defined by

$$\overline{V}_{\text{inh}}(t)n_{\text{tot}}\left\{\sigma_{\text{m}}(t)\right\} = \int_0^t V_{\text{inh}}(t-\tau)\frac{\mathrm{d}n_{\text{tot}}}{\mathrm{d}\tau}\left\{\sigma_{\text{m}}(\tau)\right\}\mathrm{d}\tau. \qquad (12)$$

Equations (11) and (12) (Denoual et al. 1997), which originate from the Poisson hypothesis, Eqn. (1), are derived in Appendix C, which makes clear that Eqn. (11) *accounts for overlaps* of inhibition zones (the derivation uses the *horizon* concept described in Fig. 5(b), which constitutes another way to look at the inhibition process). From the point of view of mathematical morphology, this model constitutes an instance of a Boolean islands model (Jeulin and Jeulin, 1981; Serra, 1982). Also, in the context of isothermal diffusive phase transformations, the three latter equations are central to the Kolmogorov-Johnson-Mehl-Avrami (KJMA) kinetic theory of nucleation and growth (Komogorov, 1937; Johnson and Mehl, 1939; Avrami, 1941). Equations (11) or (12) are valid for any density n_{tot} and any shape of interaction zones of volume V_{inh}. The present framework is thus adaptive to incorporate many different inhibition phenomenologies. In particular, the same approach can be used to analyze dynamic fragmentation of brittle materials (Grady and Kipp, 1979, 1980; Denoual and Hild, 2000; Denoual and Hild, 2002). In that case, inhibition is induced by stress relaxation around propagating cracks, as was also the case for the shell fragmentation problem studied by Mott (1947).

Bearing in mind the particular time-dependence of V_{inh} in Eqn. (9), it is observed that the time-integration in Eqn. (12) is over the nucleation time. According to our above hypothesis of considering the nucleation time as a random variable, Eqn. (12) indicates that its associated probability density at time t imposed by the Weibull-Poisson process (2) is (with $\tau \geq 0$)

$$\mathcal{P}(t_{\text{nuc}} = \tau; t) = \frac{\theta(t-\tau)}{n_{\text{tot}}\left\{\sigma_{\text{m}}(t)\right\}}\frac{\mathrm{d}n_{\text{tot}}}{\mathrm{d}\tau}\left\{\sigma_{\text{m}}(\tau)\right\}, \qquad (13)$$

where θ is the Heaviside step function.

Finally, an expression for the average void volume fraction f in the examination volume is obtained as follows. Equation (3) implies, via $a = \beta^{1/3}\,c$, the following proportionality relationship between the individual cavity volume $V_{\text{cav}} \propto a^3$ and the corresponding inhibition volume $V_{\text{inh}} \propto c^3$

$$V_{\text{cav}} = \beta\,V_{\text{inh}}. \qquad (14)$$

Using Eqn. (12), the average cavity volume $\overline{V}_{\text{cav}}$ follows as

$$\overline{V}_{\text{cav}}(t) = \beta\,\overline{V}_{\text{inh}}(t). \qquad (15)$$

Since the individual voids and inhibition zones are of same centers, they obey the same statistics. The porosity f is thus

$$f(t) = 1 - \exp\left[-\overline{V}_{\text{cav}}(t)n_{\text{tot}}\left\{\sigma_{\text{m}}(t)\right\}\right],\tag{16}$$

and simply relates to the inhibition probability by

$$f = 1 - (1 - P_{\text{inh}})^{\beta}.\tag{17}$$

This relation is illustrated by Fig. 3c, interpreting in the present context white zones as voids of overall volume fraction f, and dotted zones as inhibited zones of overall volume fraction P_{inh}.

2.3.2 Application to ramp loading

In general the number of nucleated cavities must be computed numerically. The nucleation equation (10) involves the matrix stress in the non-inhibited zones, σ_{m}. The link with the overall stress is given in Section 3.1. The computation is particularly simple for the particular case of ramp-stress loading $\sigma_{\text{m}} = \dot{\sigma}\,t$ with constant stress-rate $\dot{\sigma}$ that yields a *closed-form* solution of practical interest for experimental analyses. Upon integrating Eqn. (6) over time, and introducing the nucleation time $t_{\text{nuc}} \equiv \sigma_{\text{cav}}/\dot{\sigma}$ according to the first paragraph of Sec. 2.3.1, the individual inhibition volume (9) reads

$$V_{\text{inh}} = S\left[\frac{k\,c_P}{\alpha+1}\left(\frac{\dot{\sigma}}{\sigma_{\text{cav}}}\right)^{\alpha}(t - t_{\text{nuc}})^{\alpha+1}\right]^3\tag{18}$$

for $t > t_{\text{nuc}}$, and zero otherwise. The corresponding cavity volume V_{cav} follows from Eqn. (14).

At this stage, it proves useful to introduce a dimensionless flaw density $\widetilde{n} = n/n_c$, time $\widetilde{t} = t/t_c$, volume $\widetilde{V} = V/V_c$ and stress $\widetilde{\sigma}_{\text{m}} = \sigma_{\text{m}}/\sigma_c$. Two ways of defining those dimensionless quantities are relevant here. Both are based on the condition

$$n_c V_c = 1 \qquad (t = t_c)\tag{19}$$

that expresses the fact that some characteristic volume V_c contains *on average* one site at time t_c.

Computing P_{inh} requires identifying V_c with the *inhibition* volume, whereby the above condition reads

$$n_{\text{ci}}V_{\text{ci}} = 1, \quad n_{\text{ci}} = n_{\text{tot}}[\sigma_{\text{m}}(t_{\text{ci}})], \quad V_{\text{ci}} = V_{\text{inh}}(t_{\text{ci}}),\tag{20}$$

where the subscript ci denotes characteristic quantities associated to inhibition. A characteristic stress is defined by $\sigma_{\text{ci}} = \dot{\sigma}\,t_{\text{ci}}$. From Eqs. (2) and (20), the characteristic parameters follow as

$$t_{\mathrm{ci}} = \left[\frac{(\alpha + 1)^3 \sigma_0^m \sigma_{\mathrm{cav}}^{3\alpha}}{n_0 \left(kc_P\right)^3 S \, \dot{\sigma}^{m+3\alpha}} \right]^{\frac{1}{m+3(\alpha+1)}},$$

$$V_{\mathrm{ci}} = \left[\frac{k \, c_P \, S^{1/3} \sigma_0^{\alpha+1}}{(\alpha + 1)n_0^{(\alpha+1)/m} \sigma_{\mathrm{cav}}^{\alpha} \, \dot{\sigma}} \right]^{\frac{3m}{m+3(\alpha+1)}}, \tag{21}$$

$$\sigma_{\mathrm{ci}} = \left[\frac{(\alpha + 1)^3 \sigma_0^m \sigma_{\mathrm{cav}}^{3\alpha} \dot{\sigma}^3}{n_0 \left(kc_P\right)^3 S} \right]^{\frac{1}{m+3(\alpha+1)}}.$$

Upon carrying out the integration in Eqn. (12), Eqn. (11) reads

$$P_{\mathrm{inh}} = 1 - \exp\left[-B\big(m, 3(\alpha + 1)\big)\widetilde{t}^{\,m+3(\alpha+1)}\right], \tag{22}$$

where B is a modified Euler function of the first kind

$$B(p, q) = p \int_0^1 t^{p-1}(1 - t)^q \mathrm{d}t = \frac{\Gamma(p+1)\Gamma(q+1)}{\Gamma(p+q+1)}, \tag{23}$$

and the closed-form solution of Eqn. (10) yields

$$\begin{aligned}
\widetilde{n}_{\mathrm{nuc}}\left(\widetilde{t}\right) &= \frac{m \, B\big(m, 3(\alpha + 1)\big)^{-\frac{m}{m+3(\alpha+1)}}}{m + 3(\alpha + 1)} \\
&\times \gamma\left(\frac{m}{m + 3(\alpha + 1)}, B\big(m, 3(\alpha + 1)\big)\widetilde{t}^{\,m+3(\alpha+1)}\right),
\end{aligned} \tag{24}$$

where γ is the incomplete gamma function

$$\gamma(p, x) = \int_0^x t^{p-1}e^{-t}\mathrm{d}t \tag{25}$$

so that $\gamma(p, x \to +\infty) = \Gamma(p)$. Equation (24) is the *exact* solution to Mott's prob-
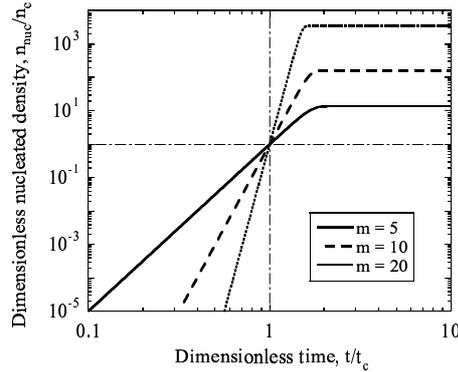

Fig. 6. Dimensionless nucleated density $\widetilde{n}_{\mathrm{nuc}}$, Eqn. (24), vs. dimensionless time $\widetilde{t}$ for three different Weibull moduli m when $\alpha = 1/2$.

lem (1947) extended to 3D cases with an initial flaw density modeled by a power law function. Figure 6 shows the change of the dimensionless density $\widetilde{n}_{\mathrm{nuc}}$ with the

dimensionless time $\widetilde{t}$. At early times $\widetilde{t} < 1$, virtually no inhibition is observed, *i.e.,* $P_{\text{inh}} \approx 0$ and $\widetilde{n}_{\text{nuc}} \approx \widetilde{n}_{\text{tot}}$. Conversely, at late times $\widetilde{t} \gg 1$, $P_{\text{inh}} \approx 1$ and saturation occurs. The higher the Weibull modulus m, the higher the density at saturation (Fig. 7).
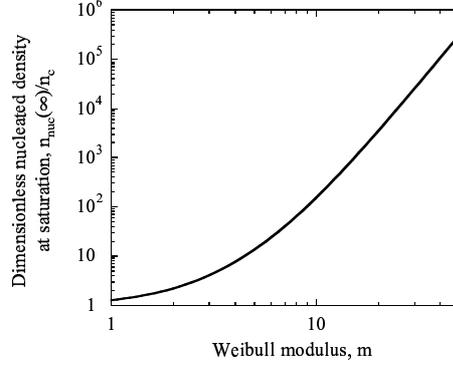

Fig. 7. Dimensionless nucleated density at saturation, $\widetilde{n}_{\text{nuc}}(\infty)$, vs. modulus m when $\alpha = 1/2$.

Computing f instead requires identifying V_c with the *void* volume, whereby the characteristic parameters obey

$$n_{\text{cc}} V_{\text{cc}} = 1, \quad n_{\text{cc}} = n_{\text{tot}}[\sigma_{\text{m}}(t_{\text{cc}})], \quad V_{\text{cc}} = V_{\text{cav}}(t_{\text{cc}}), \tag{26}$$

where the subscript 'cc' denotes characteristic quantities associated to cavities. Similarly, the characteristic stress is defined by $\sigma_{\text{cc}} = \dot{\sigma}\, t_{\text{cc}}$. Then, Eqs. (14) and (26) provide

$$t_{\text{cc}} = t_{\text{ci}} \beta^{\frac{-1}{m+3(\alpha+1)}}, \quad V_{\text{cc}} = V_{\text{ci}} \beta^{\frac{m}{m+3(\alpha+1)}}, \quad \sigma_{\text{cc}} = \sigma_{\text{ci}} \beta^{\frac{-1}{m+3(\alpha+1)}}, \tag{27}$$

and the overall porosity f, Eqn. (16), takes the form

$$f = 1 - \exp\left[-B\big(m, 3(\alpha+1)\big) \widetilde{t}^{\,m+3(\alpha+1)} \right]. \tag{28}$$

Remark that Eqs. (27) follows from replacing k by $k\beta^{1/3}$ in Eqs. (21). The only quantitative difference between Eqs. (28) and (22) resides in the definition of the characteristic parameters (*i.e.,* $\widetilde{t} = t/t_{\text{ci}}$ for inhibition and $\widetilde{t} = t/t_{\text{cc}}$ for cavities). These results are exploited below in the framework of a simplified constitutive model.

13

3 A simplified constitutive model

3.1 Homogenization approach for dynamic loadings

In usual homogenization approaches to the computation of the overall constitutive law of disordered porous media, some void spatial distribution is prescribed in advance, *all* voids being by hypothesis in mutual long-range elastic interaction, and the homogenization problem amounts to finding suitable approximation schemes for these interactions. Such approaches quite generally provide estimates of stress fluctuations in the matrix (due to pore elastic interactions), which can be considered as evenly spread in the latter. In stark contrast with this situation, the dynamical impact conditions considered here consist in loading a pristine matrix with a uniform stress state σ_{m} in the first place, this initial state being perturbed afterwards by relaxation waves originating from nucleated growing voids. As a consequence, stress fluctuations in the matrix are more localized (at least until significant overall relaxation is achieved through some "percolation" of the relaxed zones), and it should be clear that standard homogenization techniques ought not be straightforwardly transposed to this case.

The following alternative two-step approach is adopted instead, motivated by the elastic decoupling of the voids in the first stages of the spall process. In a first step, the elementary voided elastic-plastic cell of radius b, with void radius a, in which the stress is heterogeneous but equal to σ_{m} on its boundary (Fig. 3a), is replaced by an equivalent cell of radius b containing a fictitious void of radius a_{eq} (region of null stress), outside which the stress is *uniform* and equal to σ_{m} (Fig. 3b). The volume fraction of fictitious void in the equivalent cell being written $\delta(c/b)^3$, where δ is an unknown proportionality constant, it is proposed here to compute δ by requiring the elastic energy densities in the real and fictitious systems to be equal. The equation for δ thus reads

$$\frac{1}{2}\langle \sigma : \mathbb{C}^{-1} : \sigma \rangle_{\mathrm{cell}} = \left[1 - \delta(c/b)^3\right]\frac{1}{2}\frac{\sigma_{\mathrm{m}}^2}{K}, \tag{29}$$

where $\langle \cdot \rangle_{\mathrm{cell}}$ denotes a volume average over the elementary cell and where $\mathbb{C}$ is the usual (isotropic) tensor of elastic moduli built on K and μ. The lhs. of Eqn. (29), which involves microscopic hydrostatic *and* shear stress components, can be computed using the stress of the exact solution for the real elastic-plastic cell, derived in Appendix B. Since this solution also provides a and b in terms of σ_{m}, the outcome is an expression of δ as a function of σ_{m}. The associated fictitious void volume $V_{\mathrm{eq}} = Sa_{eq}^3 = \delta V_{\mathrm{inh}}$ is then introduced (it is recalled that $V_{\mathrm{inh}} = Sc^3$).

Since fictitious voids obey the same point-Poissonian statistics as real ones, the same token that was used to relate f to P_{inh} given the relationship between V_{cav} and V_{inh} in Sec. 2.3.1, can be re-used here to relate P_{inh} to an overall fictitious porosity f_{eq} given the above relationship between V_{inh} and V_{cav}. This second step

provides the macroscopic relationship analogous to Eqn. (17)

$$1 - f_{eq} = (1 - P_{\text{inh}})^{\delta}. \tag{30}$$

In the macroscopic equivalent system, the stress outside the fictitious voids is now *homogeneous everywhere*, equal to σ_{m} (Fig. 3c). Hence the expression of the macroscopic stress $\overline{\sigma}_{\text{m}}$ in terms of σ_{m} reads

$$\overline{\sigma}_{\text{m}} = (1 - f_{eq})\sigma_{\text{m}} = (1 - P_{\text{inh}})^{\delta}\sigma_{\text{m}}, \tag{31}$$

where P_{inh} and δ depend on σ_{m}. In this relation f_{eq} plays the part of an overall damage variable $\overline{D}$ in the standard relation $\overline{\sigma}_{\text{m}} = (1 - \overline{D})\sigma_{\text{m}}$ of damage theory (Lemaitre and Chaboche, 1990). To emphasize this connection the notation $\overline{D} = f_{\text{eq}}$ is used from now on.

The computation of δ from the solution of Appendix B is quite involved. Besides, Eqn. (29) is not free from arbitrariness since other energetic equivalences could be proposed that explicitly involve an additional kinetic energy term as proposed by Wang and Jiang (1994), Molinari and Mercier (2001). Bearing in mind the present exploratory purpose, a pragmatic and simplified approach is preferred that consists in considering only the limiting cases $\delta = 1$, whereby $\overline{D} = P_{\text{inh}}$, and $\delta = \beta$ whereby $\overline{D} = f$. These limits respectively provide upper and lower "pseudo-bounds" (if not rigorous ones) to $\overline{D}$. The former assumes that *relaxation is total in the plastic zone*, and neglects elastic relaxation, such that the equivalent volume is the plastic zone volume. The latter *neglects any relaxation*, such that the equivalent volume is the void volume. The relevance of these "bounds" is established below in Sec. 4.3 by comparison to experimental results.

For ramp loading, the constants required to write down in dimensionless form the equations of type (31) that stem from each "bound" have been worked out in Sec. 2.3.2. An example of the dimensionless macroscopic stress $\overline{\sigma}_{\text{m}}/\sigma_c$ as a function of the dimensionless time $\tilde{t}$, which reduces to the same master curve for both "bounds", is displayed in Fig. 8.

Completing the above approach in order to arrive at a full constitutive relation between $\overline{\sigma}_m$ and the macroscopic strain $\overline{\varepsilon}_m$ requires making additional assumptions, and is not needed here.

3.2 Spall criterion and spall strength

The *spall strength* is the quantity of primary interest in dynamic ductile damage experiments. It is defined as the maximum *macroscopic* stress $\overline{\sigma}_{\text{s}}$ sustained by the material during the damage process. Given the relationship $\overline{\sigma}_{\text{m}} = \overline{\sigma}_{\text{m}}(\sigma_{\text{m}})$ between the macroscopic stress $\overline{\sigma}_{\text{m}}$ and the microscopic stress σ_{m} in non-perturbed, uniformly
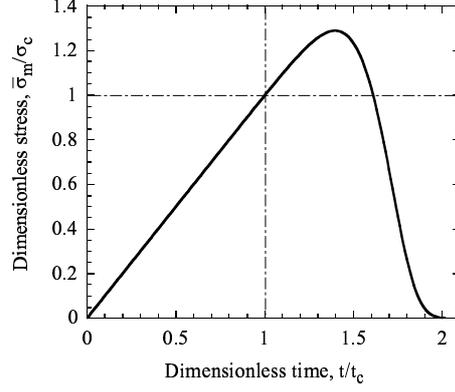
Fig. 8. Dimensionless macroscopic stress provided by Eqn. (31), vs. dimensionless time when $m = 8$ and $\alpha = 1/2$.

loaded, regions of the matrix (see Section 2.2), the macroscopic spall strength $\overline{\sigma}_s$ can be obtained as $\overline{\sigma}_s \equiv \overline{\sigma}_m(\sigma_s)$, where σ_s is the microscopic spall stress solution of

$$\frac{\mathrm{d}\overline{\sigma}_m}{\mathrm{d}\sigma_m}(\sigma_m = \sigma_s) = 0, \tag{32}$$

The spall strength $\overline{\sigma}_s$ corresponds to the maximum stress in the plot of Fig. 8. For the ramp load solution, Eqs. (22) and (31), the derivative in (32) is carried out using $t = \sigma_m/\dot{\sigma}$ and $\delta = 1$ or β in the solution. It vanishes for a dimensionless critical time for spall

$$\widetilde{t}_s = \left\{ [m + 3(\alpha + 1)]B\big(m, 3(\alpha + 1)\big) \right\}^{-1/[m+3(\alpha+1)]} \tag{33}$$

and a corresponding macroscopic spall strength

$$\overline{\sigma}_s = \sigma_c \left\{ [m + 3(\alpha + 1)]B\big(m, 3(\alpha + 1)\big)e \right\}^{-1/[m+3(\alpha+1)]}, \tag{34}$$

where $e = \exp(1)$, $\widetilde{t}_s = t/t_{cc}$, $\sigma_c = \sigma_{cc}$ for the upper "bound", and $\widetilde{t}_s = t/t_{ci}$, $\sigma_c = \sigma_{ci}$ for the lower "bound". At the spall point, the damage parameter is equal *for both "bounds"* to

$$\overline{D}_s = 1 - \exp\{-1/[m + 3(\alpha + 1)]\}. \tag{35}$$

4   Analyses of experiments on tantalum

4.1   The material

Tantalum is a transition metal of great interest for studying dynamic ductile damage mainly because of its high mass density (16660 kg/m^3), good dynamic strength and very high ductility in wide strain rate and temperature ranges. The samples used

16

herein are machined from 5 mm thick cross-rolled and fully recrystallized plates. Advanced elaboration process and heat treatment resulted in a very high purity material (99.98 wt%). The main (embrittling) impurities are 15 wt ppm O, 15 wt ppm C and less than 10 ppm N, with a homogeneous microstructure characterized by equiaxed grains of typical size 90μm, and a weak residual texture. Either optical microscopy, SEM or SIMS examinations did not reveal any localized heterogeneity down to a ~ 5 μm scale, namely, no second-phase hard particle nor impurity gradient at grain boundaries. The lack of preferable nucleation sites has been revealed by dynamic tensile tests on smooth and notched axisymmetric samples, where failure does occur in any case by ultimate thinning of the elongated ligament rather than through inclusion-induced damage, for stress triaxialities ranging from 0.3 to 1 (Roy, 2003). This material is consequently an almost ideal polycrystal for studying *homogeneous* ductile nucleation (Roy, 2003).

Mechanical properties of tantalum have been carefully determined from ultrasonic measurements, quasi-static and dynamic uniaxial testing on both as received and shocked material (Roy, 2003). During the release stage following the initial shock compression, tantalum behaves roughly as an isotropic elastic perfectly plastic medium (Roy, 2003; Juanicotena, 1998). This holds both at the macroscopic scale during release wave interaction when no damage occurs and at a mesoscopic scale around growing voids, where high strain rate gradients are roughly balanced by thermal softening at large strain. The relevant properties of tantalum in the range of stress and strain states of interest are summarized in Table 1. Twenty-two plate

Parameter	Value
Compressibility modulus K	191 GPa
Shear modulus μ	69 GPa
Mass density ρ_0	16660 kg/m^3
Yield stress Y	700 MPa

Table 1
Tantalum material parameters.

impact experiments (Nicollet et al. 2001; Roy, 2003; Llorca and Roy, 2003; Bontaz-Carion et al. 2006) were performed and/or analyzed for the present paper. Impact velocity, flyer plate material and flyer plate thickness were selected as relevant parameters for varying both shock pressure and pulse duration, and are summarized in Table 2. This essentially induces variations in the position of the plane of maximum tensile stress (the spall plane) and in the mean and maximum achievable tensile stress state along this plane. The diagnostics used to study the condition for damage and spall to occur are Doppler Laser Interferometry to record the velocity of the target free surface (overall structural response of the sample plate) and qualitative and quantitative metallurgical analyses of the soft-recovered samples. The most significant results derived from this microstructural examination have been reported elsewhere (Roy, 2003; Llorca and Roy, 2003; Nicollet et al. 2001; Bontaz-
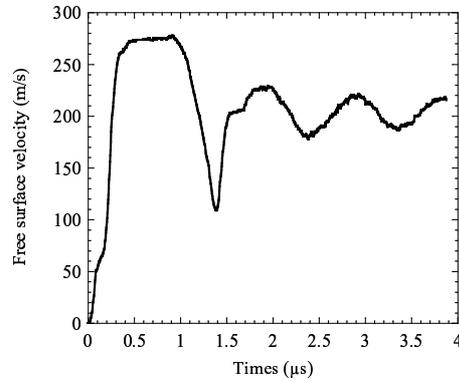
Carion et al. 2006).

Fig. 9. Example of a free-surface velocity record exhibiting a pull-back signal (Roy, 2003).

Time-resolved in situ measurements in the spall plane are not yet possible, and an inverse methodology must be adopted. As a result, data extraction is performed from free surface velocity records. In the spall plane, progressive damage induces local relaxation waves whose macroscopic consequence is a so-called *pullback signal* (see Fig. 9). For first-order estimations of relevant data (spall plane location, spall strength, critical time to fracture), a simple analytical elastic method is often used (Romanchenko and Stepanov, 1980). This method reveals successful at low shock pressure (lower than the material dynamic yield strength) or at high pressure (when elastic behavior can be neglected regarding plastic hydrodynamic component) (Meyers, 1994). This is definitely not the case for tantalum, whose dynamic yield strength (or *Hugoniot Elastic Limit*) is known to be less than an order of magnitude lower than its spall strength in the range of loading paths of interest.

Accurate data extraction requires an analysis of the complex wave pattern induced by the plate impact. One- and two-dimensional numerical simulations have consequently been performed using the Lagrangian explicit hydrocode Hesione (a proprietary code of the Commissariat à l'Énergie Atomique). In order to extract the thermomechanical fields in the region of interest (the spall plane) as accurately as possible, a tabulated equation of state and a Preston-Tonks-Wallace (2003) viscoplastic constitutive law are used (Juanicotena, 1998).

Within the relatively low shock pressure range investigated here (low temperature increase and weak plastic strain during shock and release at the macroscopic scale), these relations do predict an essentially elastic perfectly plastic behavior *during unloading*, consistent with the analytical parameters summarized in Table 1. These relations, fitted from dedicated experimental databases on shock and uniaxial compression behavior of this tantalum grade (Roy, 2003), yield very good correlation

with experimental results used in this study regarding shock and release behavior. A fracture criterion is added, leading to instantaneous mesh opening at a given tensile stress threshold (spall strength), and fitted numerically for each simulated experiment.

This numerical procedure is sufficient to extract the following data from free-surface velocity records: the stress-rate in the matrix, the critical time and the spall strength. In order for the extraction procedure to be as accurate as possible, two features are particularly sought in matching numerical results and free-surface velocity records, namely, the minimum velocity preceding pullback signal [3] and the subsequent ringing velocity frequency, which suggests efficient prediction of both spall plane position (which was compared with the experimental value for some experiments), effective maximum tensile stress and associated critical time, in a far more accurate way than using the simplified analytical method presented by Roy (2003). In this fashion, critical time (spall criterion activation) and mean tensile stress rate are derived from numerical stress history prediction at the spall plane before fracture. The corresponding values are summarized in Table 2. Associated error estimations are derived from numerical investigation of impact velocity uncertainty, mesh size, and artificial viscosity sensitivity of the calculated spall strength for some typical experiments. For some of these experiments, quantitative relevant damage activation measures were also derived using metallurgical observation of sample slices coupled with optical profilometry and image analysis (Roy, 2003) for an estimation of the three dimension damage state. In particular, the volume density of nucleated voids could be measured in the vicinity of the spall plane. These values are also given in Table 2.

4.3   Identification and validation

Figure 10 shows the change of volume density of nucleated voids n_{tot}, Eqn. (2), as a function of the shock pressure. This plot is restricted to data obtained from shots A1–A5, A7, A9, A12 and B8 only. These shots involve only moderate pressures so that void coalescence presumably remains limited. Moreover, in the impact configurations considered, the shock pressure is equal to the negative of σ_{m}, the maximum stress in the matrix, which takes place in non-inhibited regions that exist whenever coalescence is marginal. The assumption of a constant stress rate pulse (*i.e.,* ramp load) is applied to tantalum to determine the Weibull parameters of Eqn. (2). The best power-law fit displayed in Fig. 10 provides an exponent $m = 8$, a moderate

---

[3]   We emphasize that a completely fractured plane at the macroscopic scale is not a necessary condition for pullback-type free surface velocity evolution, as highlighted by Llorca and Roy (2003) and Roy (2003). Primary internal energy release leading to pullback velocity (early re-acceleration) has been experimentally shown to be initiated in the vicinity of the spall plane at a given low incipient damage level. This is consistent with the basic hypothesis of the spall criterion developed in part 3.

	Experimental					Impact simulations			
	Target	Imp.	Imp.	Impact	Void density	Shock	Spall strength	Stress rate	Critical time
Shot	thick.	nature	thick.	vel.		press.			
	mm		mm	m.s^{-1}	number / mm^3	GPa	GPa	GPa/μs	μs
	± 0.01		± 0.01	$\pm 2.0\%$	$\pm 30\%$	$\pm 5\%$	$\pm 5\%$	$\pm 12\%$	$\pm 17\%$
A1	4.95	CuC2	3.00	252	256	5.5	N/A	N/A	N/A
A2	4.95	CuC2	1.00	271	60	5.8	N/A	N/A	N/A
A3	4.95	CuC2	2.00	270	N/A	5.87	5.32	17	0.36
A4	4.95	CuC2	2.00	270	75	5.87	N/A	N/A	N/A
A5	4.95	CuC2	4.00	268	301	5.88	5.37	11	0.48
A6	4.95	CuC2	3.00	269	N/A	5.9	5.32	15	0.34
A7	4.95	Ta	3.00	207	340	5.93	5.1	15	0.32
A8	4.95	Ta	3.00	303	N/A	8.9	6.6	42.8	0.15
A9	4.95	Ta	3.00	306	3660	9.01	6.6	49.7	0.12
A10	4.95	Ta	3.00	307	N/A	9.01	6.6	53.6	0.12
A11	4.95	Ta	3.00	415	N/A	12.5	7.5	81.1	0.08
A12	4.95	Ta	3.00	424	150000	12.7	N/A	N/A	N/A
B1	3.96	AU4G (Al 2017)	3.97	412	N/A	4.92	N/A	9.1	N/A
B2	3.92	AU4G (Al 2017)	3.49	481	N/A	5.86	5.35	17.3	0.38
B3	3.96	AU4G (Al 2017)	1.99	570	N/A	6.5	5.9	16.2	0.34
B4	3.94	AU4G (Al 2017)	3.01	551	N/A	6.89	6.15	26.9	0.24
B5	3.93	AU4G (Al 2017)	3.50	654	N/A	8.3	7.05	44.7	0.16
B6	3.96	AU4G (Al 2017)	4.01	528	N/A	8.55	7.1	47	0.15
B7	3.99	AU4G (Al 2017)	3.99	671	N/A	9.06	7.2	106.4	0.07
B8	3.95	AU4G (Al 2017)	0.49	1039	2250	9.06	7.2	106.4	0.07
B9	3.90	AU4G (Al 2017)	3.49	900	N/A	11.95	7.9	99.9	0.07
B10	3.96	AU4G (Al 2017)	3.48	1110	N/A	15.25	7.05	80	0.04

Table 2

Parameters of shock experiments. Shots A1–A12 (resp. B1–B10) are those of Roy (2003) and Llorca and Roy (2003) (resp. Nicollet et al. (2001) and Bontaz-Carion et al. (2006)). Third row: standard uncertainties. Sixth column: voids densities measured by image analysis on recovered samples. *N/A* indicates unavailable data.

value indicative of weak scatter in nucleation levels. A value of $\sigma_0 = 700$ MPa for the scaling stress equal to elastic limit is used, whence the density $n_0 = 7.9 \times 10^{-6}$ mm^{-3} is obtained. Upper and lower theoretical "bounds" for the critical time ver-
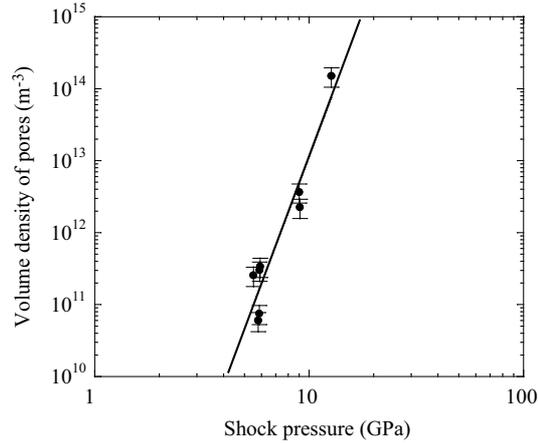

Fig. 10. Volume density of pores n_{tot} vs. shock pressure for tantalum. The solid symbols are experimental points and the line is the best fit of Eqn. (2).

sus stress rate obtained from (33) with $\alpha = 1/2$ and $m = 8$ are displayed in Fig. 11.
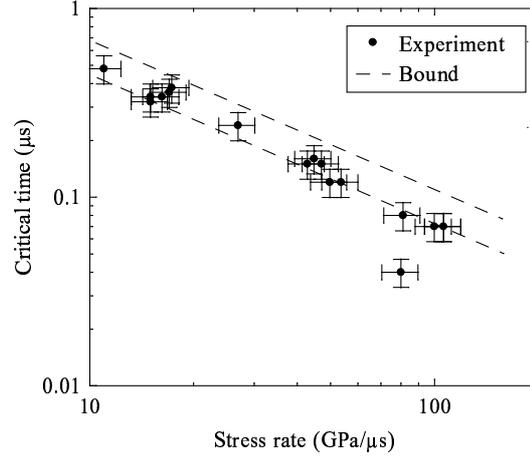
Fig. 11. Critical time vs. stress rate. The solid symbols are experimental points and the dashed lines are the "bounds" built from Eqn. (33) with $\alpha = 1/2$, and $m = 8$ determined from Fig. 10.

Almost all experimental points are seen to lie within these "bounds". Besides the overall trend is consistent with the slope of the latter. Likewise, upper and lower theoretical bounds derived from (34) with $\alpha = 1/2$ and $m = 8$ are compared to experimental data in Fig. 12 in log-log scale, which illustrates the power-law increase of the spall strength with the stress rate. Though the experimental points are linearly correlated with a slope lower than that of the bounds, they lie between the latter in the considered range of loadings, which is quite satisfactory. Thus, the rate sensitivity of the spall strength can be described by the present model with no need to incorporate a time-dependent constitutive equation of the matrix.
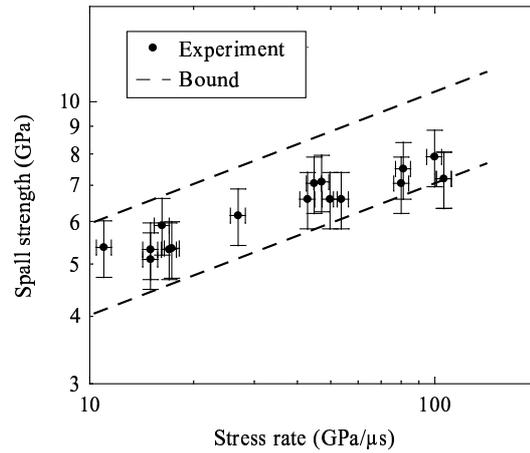

Fig. 12. Spall strength vs. stress rate for tantalum. The solid symbols are experimental points and the dashed lines are the bounds built from Eqs. (33) and (34) with $\alpha = 1/2$, and $m = 8$ determined from Fig. 10.

21

5 Analyses of data on aluminum and magnesium

Kanel et al. (1996) performed experiments on aluminum and magnesium. In both cases, the spall strength was shown to be approximated by a power-law of the strain rate. In the present analysis, as in all the developments derived herein, the effect of the temperature is ignored. Consequently, only experiments performed at ambient are considered. By using $\sigma_s = \dot{\sigma}\, t_s = \tilde{t}_s \dot{\sigma}\, t_c \propto \dot{\sigma}\, t_c$, any of Eqs. (21) or (27) for t_c vs. $\dot{\sigma}$, and the proportionality $\dot{\sigma} \propto \dot{\varepsilon}$ (of elastic origin, and legitimate in non-relaxed regions of uniform σ_m), the following strain-rate dependence is obtained for the microscopic spall strength

$$\sigma_s \propto \dot{\epsilon}^{\eta} \tag{36}$$

with

$$\eta = \frac{3}{m + 3(\alpha + 1)} \tag{37}$$

where $\dot{\epsilon}$ denotes the average strain rate in the experiments. In this expression, the only unknown is the modulus m, provided a value of $\alpha = 1/2$ is chosen as in the previous experiments on tantalum. For aluminum, a value $\eta = 0.059$ is found, which would lead to a value of $m = 46$ and for magnesium, $\eta = 0.072$ so that $m = 37$. These two (high) values of m are an indication of a small scatter in terms of nucleation level when compared to tantalum (Table 3) for which a gradual and scattered nucleation was observed.

Parameter	Tantalum	Aluminum	Magnesium
α	0.5	0.5	0.5
Weibull modulus m	8	46	37

Table 3
Nucleation parameters for tantalum, aluminum and magnesium.

6 Conclusion and perspectives

We proposed a probabilistic model for nucleation and growth in ductile fracture, using Poisson-Weibull statistical concepts, which are usually applied to brittle materials. We showed, through analyses of several sets of experimental data in spall experiments, that these concepts are well-suited to describing ductile fracture as well. In particular, we arrived at a simple explanation for the power-law dependence of the spall strength vs. strain-rate observed by Kanel et al. (1996). The proposed model makes use of a velocity-dependent extension of the concept of cavitation stress in metals. Though it has been presented, for simplicity, in the framework of ideal plasticity, expressions of cavitation thresholds that account for hardening are available (Mandel, 1966; Bishop and Hill, 1945), and could be easily appealed

to. Investigations of the influence of hardening on the present nucleation theory, as well as that of viscoplastic behavior, are left to future work. Also, next steps should consist in implementing the full model in a finite-element hydrocode, and in extending its range of validity to the coalescence regime.

7 Acknowledgments

References

[1] Avrami, M., 1941. Kinetics of Phase Change. III. Granulation, Phase Change, and Microstructure. J. Chem. Phys. 9, 177–184.

[2] Bishop, R. F., Hill, R., and Mott, N. F., 1945. The Theory of Indentation and Hardness Tests. Proc. Phys. Soc., 57 (3), 147–159.

[3] Bontaz-Carion, J., and Pellegrini, Y.-P., 2006. X-Ray Microtomography Analysis of Dynamic Damage in Tantalum. Adv. Engng. Mat., 8 (6), 480-486.

[4] Cahn, J. W., 1996. The Time-Cone Method for Nucleation and Growth Kinetics on a Finite Domain, in *Proc. MRS Symp. on Thermodynamics and Kinetics of Phase Transformations (Boston, MA, 1995)* 398 (Mat. Res. Soc., Pittsburgh), pp. 425–438.

[5] Carroll, M. M., and Holt, A. C., 1972. Static and Dynamic Pore collapse Relations for Ductile Porous Materials. J. Appl. Phys. 43(4), 1626–1636.

[6] Cortes, R., 1992. The Growth of Microvoids under Intense Dynamic Loading. Int. J. Solids Struct., 29 (11), 1339–1350.

[7] Curran, D. R., Seaman, L., and Shockey, D. A., 1987. Dynamic Failure of Solids. Phys. Rep., 147, 253–388.

[8] Czarnota, C., Mercier, S., and Molinari, A., 2006. Modelling of Nucleation and Void Growth in Dynamic Pressure Loading, Application to Spall Test on Tantalum. Int. J. Fracture, 141 (1-2), 177–194.

[9] Czarnota, C., Jacques, N., Mercier, S., and Molinari, A., 2008. Modelling of dynamic ductile fracture and application to the simulation of plate impact tests on tantalum. J. Mech. Phys. Solids, 56, 1624-1650.

[10] Davies, D. G. S., 1973. The Statistical Approach to Engineering Design in Ceramics. Proc. Brit. Ceram. Soc., 22, 429-452.

[11] Denoual, C., Barbier, G., and Hild, F., 1997. A Probabilistic Approach for Fragmentation of Brittle Materials under Dynamic Loading, C. R. Acad. Sci. Paris - Series IIB, 325 (12), 685–691.

[12] Denoual, C., 1998. *Approche probabiliste du comportement à l'impact du car-*

bure de silicium : application aux blindages moyenne énergie. Ph.D. Thesis, École Normale Supérieure de Cachan, France.

[13] Denoual, C., and Hild, F, 2000. A Damage Model for the Dynamic Fragmentation of Brittle Solids. Comp. Meth. Appl. Mech. Eng., 183 (3–4), 247–258.

[14] Denoual, C., and Diani, J. M., 2002. Cavitation in Compressible Visco-Plastic Materials. in *Shock Compression of Condensed Matter-2001: 12th APS Topical Conference*, AIP Conf. Proc. Vol. 620 (1), pp. 495–498.

[15] Denoual, C., and Hild, F., 2002. Dynamic Fragmentation of Brittle Solids: A Multi-Scale Model. Eur. J. Mech. – A/Solids, 21 (1), 105–120.

[16] Dragon, A., and Trumel, H., 2003. Damage under Impact Loading - Some Modelling Challenges. In *Proc. Fifth Int. Symp. High Dynamic Pressures (HDP V), June 23-27, 2003, Saint-Malo, France*, Vol. 1, CEA / Institut Français de Pyrotechnie, Paris, pp. 267–283.

[17] Eftis, J., and Nemes, J. A., 1991. Evolution Equation for the Void Volume Growth Rate in a Viscoplastic-Damage Constitutive Model. Int. J. Plast., 7 (4), 275–293.

[18] Forrestal, M. J., and Luk, V. K., 1988. Dynamic Spherical Cavity-Expansion in a Compressible Elastic-Plastic Solid. J. Appl. Mech., 55 (2), 275–279.

[19] Glennie, E. B., 1972. The Dynamic Growth of a Void in a Plastic Material and an Application to Fracture. J. Mech. Phys. Solids, 20 (6), 415–429.

[20] Grady, D. E., and Kipp, M. E., 1979. The Micromechanics of Impact Fracture of Rock. Int. J. Rock Min. Sci. & Geomech. Abstr., 16, 293–302.

[21] Grady, D. E., and Kipp, M. E., 1980. Continuum Modeling of Explosive Fracture in Oil Shale. Int. J. Rock Min. Sci. & Geomech. Abstr., 17, 147–157.

[22] Grady, D. E., 1988. The Spall Strength of Condensed Matter. J. Mech. Phys. Solids, 36 (3), 353–384.

[23] Gulino, R., and Phoenix, S. L., 1991. Weibull Strength Statistics for Graphite Fibres Measured from the Break Progression in a Model Graphite / - Glass / Epoxy Microcomposite. J. Mater. Sci., 26 (11), 3107–3118.

[24] Gurson, A. L., 1977. Continuum Theory of Ductile Rupture by Void Nucleation and Growth. Part I. Yield Criteria and Flow Rules for Porous Ductile Media. J. Engng. Mat. Technol., 99, 2–15.

[25] Hopkins, H. G., 1960. Dynamic Expansion of Spherical Cavities in Metals. In *Progress in Solid Mechanics*, I. N. Sneddon, and R. Hill, eds., North Holland, Amsterdam, Vol. 1, pp. 84–164.

[26] Hou, H.-S., and Abeyaratne, R., 1992. Cavitation in Elastic and Elastic-Plastic Solids. J. Mech. Phys. Solids, 40 (3), 571–592.

[27] Hunter, S. C., and Crozier, R. J. M., 1968. Similarity Solution For the Rapid Uniform Expansion of a Spherical Cavity in a Compressiblle Elastic-Plastic Solid. Quart. J. Mech. Appl. Math., 21 (4), 467–486.

[28] Jeulin, D., and Jeulin, P., 1981. Synthesis of Rough Surfaces by Random Morphological Functions. In *Procs. 3rd European Symposium of Stereology*, pp. 239–246.

[29] Jeulin, D., 1991. *Modèles morphologiques de structures aléatoires et changement d'échelle*. Thèse d'État, Caen University, France.

[30] Johnson, W.A., and Mehl, R.F., 1939. Reaction Kinetics in Processes of Nucleation and Growth. Trans. Am. Inst. Min. Metall. Eng. 135, 416–458.

[31] Juanicotena, A., 1998. *Étude théorique et expérimentale du comportement viscoplastique des matériaux aux grandes déformations et grandes vitesses de déformation. Application à l'acier Mars 190 et au tantale*, Ph.D. Thesis, Metz University, France.

[32] Kanel, G. I., Razorenov, S. V., Bogatch, A., Utkin, A. V., Fortov, V. E., and Grady, D. E., 1996. Spall Fracture Properties of Aluminum and Magnesium at High Temperatures J. Appl. Phys., 79 (11), 8310–8317.

[33] Kolmogorov, A.N., 1937. On the Statistical Theory of Metal Crystallization. Izv. Akad. Nauk. SSSR, Ser. Matemat. 3, 355–360 (in Russian). English translation (1992): *Selected works of A.N. Kolmogorov, Vol. II*, A. N. Shiryayev, ed., Kluwer Academic, Dordrecht, pp. 188–192.

[34] Lemaitre, J., Chaboche, J.-L., 1990. *Mechanics of Solid Materials*, Cambridge University Press, Cambridge.

[35] Llorca, F., and Roy, G., 2003. Metallurgical investigations of dynamic damage in tantalum. In *Shock Compression of Condensed Matter-2003: 12th APS Topical Conference*, AIP Conf. Proc. Vol. 706, pp. 589–592.

[36] Mandel, J., 1966. *Cours de mécanique des milieux continus. Tome I : Généralités, Mécanique des fluides*, and *Tome II : Mécanique des solides*, Gauthier-Villars, Paris.

[37] Meyers, M. A., and Aimone, C. T., 1983. Dynamic Fracture (Spalling) of Metals. Prog. Mater. Sci., 18 (1), 1–96.

[38] Meyers, M. A., 1994. *Dynamic Behavior of Materials* J. Wiley and Sons, New York.

[39] Molinari, A., and Mercier, S., 2001. Micromechanical Modelling of Porous Materials under Dynamic Loading. J. Mech. Phys. Solids, 49 (7), 1497–1516.

[40] Molinari, A., and Wright, T. W., 2005. A Physical Model for Nucleation and Early Growth of Voids in Ductile Materials Under Dynamic Loading. J. Mech. Phys. Solids, 53 (7), 1476–1504.

[41] Mott, N. F., 1947. Fragmentation of Shell Cases. Proc. Roy. Soc. London A, 189, pp. 300-308.

[42] Nicollet, M., Manczur, P., Redasse, J.-C., and Rion, C., 2001. *Synthèse des résultats des expériences d'endommagement d'échantillons de tantale*, unpublished CEA data.

[43] Ortiz, M., and Molinari, A., 1992. Effect of Strain Hardening and Rate Sensitivity on the Dynamic Growth of a Void in a Plastic Material. J. Appl. Mech., 59 (1), 48–53.

[44] Preston, D. L., Tonks, D. L., and Wallace, D. C., 2003. Model of plastic deformation for extreme loading conditions. J. Appl. Phys., 93 (1), 211–220.

[45] Romanchenko, V. I., and Stepanov, G. V., 1980. Dependence of the Critical Stresses on the Loading Time Parameters During Spall in Copper, Aluminum and Steel. J. Appl. Mech. Techn. Phys., 21 (4), 555–561.

[46] Roy, G., Dragon, A., Trumel, H., and Llorca, F., 2002. Spall Damage Modelling. Inertia Effects in Fully Elastic Plastic Range. In *Proc. 9th International*

Symposium on plasticity and its current applications (Plasticity 2002), A. S. Khan and O. Lopez-Pamies, eds., Aruba, The Netherlands, pp. 666–668.

[47] Roy, G., 2003. *Vers une modélisation approfondie de l'endommagement dynamique ductile. Investigation expérimentale d'une nuance de tantale et développements théoriques*, Ph.D. Thesis, Poitiers University, France.

[48] Rudd, R. E., and Belak, J. F., 2002. Void Nucleation and Associated Plasticity in Dynamic Fracture of Polycrystalline Copper: an Atomistic Simulation. Comput. Mater. Sci., 24 (1-2), 148–153.

[49] Serra, J., 1982. *Image Analysis and Mathematical Morphology*, Academic Press, London.

[50] Thomason, P. F., 1999. Ductile Spallation Fracture and the Mechanics of Void Growth and Coalescence under Shock-Loading Conditions. Acta Mater., 47 (13), 3633–3646.

[51] Tong, W., and Ravichandran, G., 1995. Inertial effects on void growth in porous viscoplastic materials. J. Appl. Mech., 62 (3), 633–639.

[52] Tonks, D. L., Zurek, A. K., and Thissel, W. R., 2001. Modelling Incipient Spallation in Commercially Pure Tantalum. In *Fundamental Issues and Applications of Shock-Wave and High Strain-Rate Phenomena, EXPLOMET 2000*, K. P. Staudhammer, L. E. Murr, and M. A. Meyers, eds., Elsevier, New York, pp. 517–523.

[53] Tvergaard, V., 1999. Effect of Large Elastic Strains on Cavitation Instability Predictions for Elastic-Plastic Solids. Int. J. Solids Struct., 36 (35), 5453–5466.

[54] Wang, Z.-P., and Jiang, Q., 1997. A Yield Criterion for Porous Ductile Media at High Strain-Rate. J. Appl. Mech., 64 (3), 503–509.

[55] Weibull, W., 1951. A Statistical Distribution Function of Wide Applicability. J. Appl. Mech., 18, 293–297.

[56] Wu, X. Y., Ramesh, K. T., and Wright, T. W., 2003. The Dynamic Growth of a Single Void in a Viscoplastic Material under Transient Hydrostatic Loading, J. Mech. Phys. Solids, 51 (1), 1–26.

[57] Zelodovich, Y. B., and Raizer, Y. P., 2002. *Physics of Shock Waves and High-Temperature Hydrodynamic Phenomena*, Dover, New York, p. 743.

A Weibull distribution

The probability of finding *at least* one nucleation site (*i.e.,* the "weakest link") in a uniformly loaded domain Ω is

$$P(N \geq 1, \Omega) = 1 - P(N = 0, \Omega) = 1 - e^{-V\, n_0 (\langle \sigma_{\mathrm{m}} \rangle / \sigma_0)^m}. \qquad \text{(A.1)}$$

When the domain is not uniformly loaded, we instead have

$$P(N \geq 1, \Omega) = 1 - e^{-V_{\mathrm{eff}}\, n_0 (\langle \sigma_M \rangle / \sigma_0)^m}, \qquad \text{(A.2)}$$

26

where V_{eff} denotes the effective volume (Davies, 1973)

$$V_{\text{eff}} = \int_\Omega \mathrm{d}^3x \left[\frac{\sigma_{\text{m}}(\mathbf{x})}{\sigma_{\text{M}}}\right]^m \quad \text{with} \quad \sigma_{\text{M}} = \max_\Omega \sigma_{\text{m}}(\mathbf{x}). \tag{A.3}$$

Equations (A.1) and (A.2) are the Weibull model (Weibull, 1939) written in the context of ductile damage (see also Czarnota et al. 2006).

B Derivation of Eqns. (3) and (4)

B.1 Preliminaries

We detail here the steps leading to Eqns. (3) and (4), in the stationary growth regime studied by Forrestal and Luk (1988). In this one-dimensional spherical approach, a cavity of radius $a(t)$ grows at constant velocity $\dot{a}$ in an infinite elasto-plastic medium submitted to an initially uniform hydrostatic stress state $\sigma_{\text{m}}(t)$. This growth perturbs the stress field within a partially relaxed volume of radius $r = b(t) \equiv c_L\, t$, where $c_L = \sqrt{(K + 4\mu/3)/\rho_0}$ is the velocity of longitudinal elastic waves. The front $b(t)$ separates the outer medium at rest in a state of uniform stress, from the inner perturbed region expanding with the growing void. The inner region is divided into an external elastic shell $c(t) \leq r \leq b(t)$, and a shell at yield which surrounds the cavity, $a(t) \leq r \leq c(t)$.

In the steady-state growth regime where $c(t) = \dot{c}t$, a self-similar solution for the radial displacement u is sought for in the form $u(r,t) = c(t)\,\widetilde{u}(\xi)$. There, $\xi(r,t) = r/c(t)$ is the scaled radial coordinate, and $\widetilde{u}(\xi)$ is the scaled displacement. Moderate stress is assumed so as to neglect: (i) density variations in the elastic shell, (ii) nonlinear elasticity, and (iii) convection terms (Forrestal and Luk, 1988). Using $\dot{\xi} = -\xi\,\dot{c}/c$, the velocity and acceleration read

$$\dot{u} = (\widetilde{u} - \xi\,\widetilde{u}')\,\dot{c}, \tag{B.1}$$
$$\ddot{u} = \xi^2\widetilde{u}''\,\dot{c}^2/c. \tag{B.2}$$

Equation (B.1) provides the scaled velocity $\widetilde{v}(\xi) \equiv \dot{u}(r,t)/\dot{c}$.

For further use, we introduce the scaled yield stress, shear modulus, applied hydrostatic stress, and density respectively as: $y \equiv Y/K$, $g \equiv 2\mu/K$, $\widetilde{\sigma}(t) \equiv \sigma_{\text{m}}(t)/K$, $\widetilde{\rho}(\xi) \equiv \rho(r,t)/\rho_0$, where ρ_0 is the reference material density. In usual metals,

$$y \ll g \lesssim 1. \tag{B.3}$$

B.2 Elastic shell

Combining linear elasticity relationships and the momentum equation

$$\partial_r \sigma_r + (2/r)(\sigma_r - \sigma_\theta) = \rho \ddot{u},$$

where σ_r and σ_θ are respectively the radial and hoop stresses, and introducing $\gamma_L \equiv \dot{c}/c_L$, yields the differential equation

$$\left(1 - \gamma_L^2 \, \xi^2\right) \widetilde{u}'' + \left(2/\xi^2\right) \left(\xi \, \widetilde{u}' - \widetilde{u}\right) = 0. \tag{B.4}$$

Its solution is of the form $\widetilde{u}(\xi) = C^{(1)}\xi + C^{(2)}(1 - 3\gamma_L^2 \, \xi^2)/\xi^2$, where the integration constants $C^{(1,2)}$ are found from boundary conditions. The first one is $\widetilde{u}(\xi = 1/\gamma_L) = \sigma_{\mathrm{m}}/(3K\gamma_L)$, and stems from the applied external boundary traction. The second one is $\widetilde{u}(\xi)/\xi - \widetilde{u}'(\xi)|_{\xi=1} = Y/(2\mu)$, which expresses the yield condition $\sigma_\theta - \sigma_r = Y$ (tensile case) at the elastic-plastic boundary. The solution for $\xi \in (1, 1/\gamma_L)$ is then

$$\widetilde{u}^e = \frac{\widetilde{\sigma}}{3}\xi + \frac{Y}{6\mu} \frac{(1 - \gamma_L \, \xi)^2 (1 + 2\gamma_L \, \xi)}{(1 - \gamma_L^2) \, \xi^2}. \tag{B.5}$$

Denoting by ν the Poisson ratio, the corresponding radial stress reads

$$\sigma_r^e = \widetilde{\sigma} - \frac{2y}{3} \frac{(1 - \gamma_L \, \xi) \left[(1 - 2\nu)(1 + \gamma_L \, \xi) + (1 + \nu)\gamma_L^2 \, \xi^2\right]}{(1 - 2\nu) \, (1 - \gamma_L^2) \, \xi^3}. \tag{B.6}$$

B.3 Plastic shell

Mass conservation, namely, $\partial_t \rho + [\partial_r + (2/r)](\dot{u} \, \rho) = 0$, provides

$$\widetilde{v}' + (2/\xi)\widetilde{v} = (\xi - \widetilde{v}) \, \widetilde{\rho}'/\widetilde{\rho}. \tag{B.7}$$

Introduce now the plastic velocity $c_P = \sqrt{K/\rho_0}$, and (after γ_L) another scaling of $\dot{c}$ as $\gamma_P \equiv \dot{c}/c_P$. The yield condition $\sigma_\theta - \sigma_r = Y$, combined with linear elasticity in the form $\mathrm{Tr}\,\sigma = \sigma_r + 2\sigma_\theta = 3K \, (\rho_0/\rho - 1)$, gives

$$\partial_r \sigma_r = -K \left(\rho_0/\rho^2\right) \partial_r \rho. \tag{B.8}$$

Using (B.8) in the momentum equation then provides

$$\xi \, \widetilde{\rho}' = \left(\gamma_P^2 \, \xi^2 \, \widetilde{v}' \, \widetilde{\rho} - 2y\right) \widetilde{\rho}^2. \tag{B.9}$$

Eliminating $\widetilde{\rho}'(\xi)$ from Eqns. (B.7) and (B.9) then yields

$$\left[1 - \xi \gamma_P^2 \, \widetilde{\rho}^2 \, (\xi - \widetilde{v})\right] \widetilde{v}' + 2 \, (1 - y \, \widetilde{\rho}) \, (\widetilde{v}/\xi) = -2y \, \widetilde{\rho}. \tag{B.10}$$

28

Equations (B.9) and (B.10) constitute a system for $\widetilde{\rho}$ and $\widetilde{v}$, should variations in ρ be accounted for. Upon neglecting their higher-order influence in $\widetilde{v}$ at moderate stress, and assuming $y \ll 1$, see (B.3), Eqn. (B.10) reduces to

$$\left(1 - \gamma_P^2 \, \xi^2\right) \widetilde{v}' + 2(\widetilde{v}/\xi) = -2y. \tag{B.11}$$

Note that this equation also assumes that $\widetilde{v}(\xi) \ll \xi$, which is satisfied if the material velocity is much lower than the velocity of the void boundary. However, finite-element calculations of void expansion (Roy, 2003) indicate that this assumption is expected to hold everywhere except near the void boundary where the velocity gradient is highest. The difference induced by neglecting this term on the overall behavior is small anyway (Forrestal and Luk, 1988; Roy, 2003), see Fig. B.1 below.

Continuity of the material velocity at the elastic-plastic interface provides the boundary condition $\widetilde{v}(1) = y/g$. Then, the solution of Eqn. (B.11) in the interval $\xi \in (a/c, 1)$ is

$$\widetilde{v}^p(\xi) = \frac{y}{\gamma_P^2 \, \xi^2} \left[\frac{1 - \gamma_P^2 \, \xi^2}{1 - \gamma_P^2}(1 + \gamma_P^2/g) - \xi \right]$$
$$+ \frac{y}{2\gamma_P^3 \, \xi^2}(1 - \gamma_P^2 \, \xi^2) \log \frac{(1 + \gamma_P \, \xi)(1 - \gamma_P)}{(1 - \gamma_P \, \xi)(1 + \gamma_P)}. \tag{B.12}$$

With $\alpha_P \equiv \dot{a}/c_P$ the scaled void growth velocity, the radial stress in the same interval reads, upon integrating (B.8) and using (B.7) under the above approximations

$$\widetilde{\sigma}_r^p(\xi) = 2y \frac{(\gamma_P \, \xi - \alpha_P)(1 + \gamma_P^2/g)}{(1 - \gamma_P^2)\alpha_P \, \xi}$$
$$+ y \left[\log \frac{\gamma_P^2 \, \xi^2(1 - \alpha_P^2)}{\alpha_P^2(1 - \gamma_P^2 \, \xi^2)} - \frac{1}{\gamma_P \, \xi} \log \frac{(1 + \gamma_P \, \xi)(1 - \gamma_P)}{(1 - \gamma_P \, \xi)(1 + \gamma_P)} \right.$$
$$\left. + \frac{1}{\alpha_P} \log \frac{(1 + \alpha_P)(1 - \gamma_P)}{(1 - \alpha_P)(1 + \gamma_P)} \right]. \tag{B.13}$$

B.4 Complete and approximate solutions

The equations for the void growth velocity then consist in the relations $\alpha_P = \gamma_P \, \widetilde{v}^p(\xi = a/c)$ and $\widetilde{\sigma}_r^e(1) = \widetilde{\sigma}_r^p(1)$. The first one reads

$$\alpha_P \frac{\alpha_P^2/y + 1}{1 - \alpha_P^2} = \gamma_P \frac{\gamma_P^2/g + 1}{1 - \gamma_P^2} + \frac{1}{2} \log \frac{(1 + \alpha_P)(1 - \gamma_P)}{(1 - \alpha_P)(1 + \gamma_P)}, \tag{B.14}$$
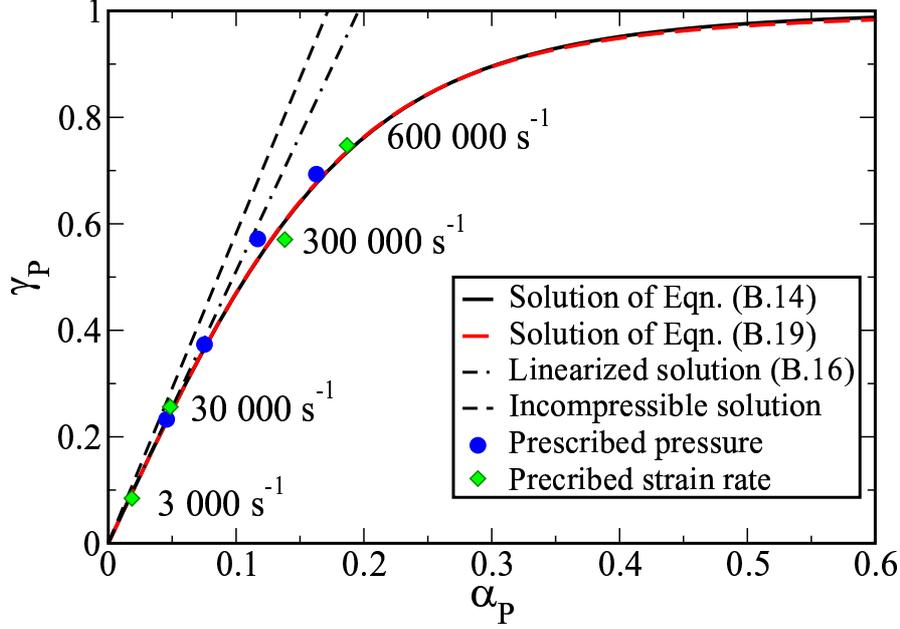
29

Fig. B.1. Dimensionless velocity $\gamma_P = \dot{c}/c_P$ of the plastic zone vs. dimensionless growth velocity $\alpha_P = \dot{a}/c_P$ of a cavity in a compressible and incompressible medium (the value of c_P at finite compressibility is used for all curves). Material parameters of tantalum (Table 1), except for the bulk modulus in the incompressible case.

whereas, setting $\kappa \equiv c_L/c_P = (1 + 2g/3)^{1/2}$, the second one yields

$$
\begin{aligned}
\frac{\widetilde{\sigma}}{y} =& \frac{2}{3} + 2\frac{\kappa^2 \gamma_P^2/g}{1 + \kappa\,\gamma_P} + 2\frac{\gamma_P^2/g + 1}{1 - \gamma_P^2}\left(\frac{\gamma_P}{\alpha_P} - 1\right) \\
&+ \frac{1}{\alpha_P} \log \frac{(1 + \alpha_P)(1 - \gamma_P)}{(1 - \alpha_P)(1 + \gamma_P)} + \log \frac{\gamma_P^2(1 - \alpha_P^2)}{\alpha_P^2(1 - \gamma_P^2)}.
\end{aligned}
\tag{B.15}
$$

Seeking low-order expansions of Eqns. (B.14) and (B.15), $\dot{a}$ is computed as a function of σ_{m} by first looking for a solution of Eqn. (B.14) in the perturbative form $\gamma_P = \sum_{k \geq 1} A_k \alpha_P^k$, where the unknowns A_k are determined order-by-order. To leading order in α_P, the solution is

$$
\gamma_P \simeq \beta^{-1/3}\,\alpha_P, \quad \beta \equiv \frac{y(g + 3/2)}{g(y + 3/2)} \simeq \frac{Y}{2\mu} + \frac{2Y}{3K},
\tag{B.16}
$$

where the approximated value of β stems from (B.3). Next, inserting the expansion into Eqn. (B.15), assuming a relationship $\widetilde{\sigma}(\alpha_P) = \widetilde{\sigma}_c + \sum_{k \geq 1} B_k \alpha_P^k$ where $\widetilde{\sigma}_c$ and the B_k are unknowns, and again simplifying the coefficients with (B.3), yields

$$
\widetilde{\sigma} = \frac{2y}{3}(1 - \log \beta) + \left[2 - O\left((yg^2)^{1/3}\right)\right]\alpha_P^2 + O\left(\alpha_P^3\right),
\tag{B.17}
$$

where the orders of the neglected terms are indicated. Hence $B_2 = 2$ in the incompressible limit. We do not reproduce its full expression, quite involved but easily

retrieved with a symbolic calculator. The first term in the r.h.s. is the scaled cavitation stress, $\tilde{\sigma}_{\text{cav}} = \sigma_{\text{cav}}/K$, first computed by Bishop, Hill and Mott [4] (1945), and later on by Mandel (1966) for finite compressibility under the form $\sigma_{\text{cav}} = (2Y/3)\{1 + \log E/[3(1-\nu)Y]\}$, E being Young's modulus.

Growth occurs only if $\sigma_{\text{m}} > \sigma_{\text{cav}}$. Hence from (B.17), for $\sigma_{\text{m}} \gtrsim \sigma_{\text{cav}}$, the pore growth velocity behaves as

$$\dot{a} \sim \dot{a}_0(\sigma_{\text{m}}/\sigma_{\text{cav}} - 1)^{1/2}, \tag{B.18}$$

where $\dot{a}_0 \equiv [\sigma_{\text{cav}}/(B_2\,\rho_0)]^{1/2}$ is a characteristic pore growth velocity of the material with $B_2 \simeq 2$. Using the full expressions of β and B_2, we obtain for Al, Cu and Ta: $\dot{a}_0 \simeq 289$, 224 and 145 m/s respectively, and $\sigma_{\text{cav}} \simeq 0.11$, 0.89, and 2.75 GPa respectively. For comparison purposes, we note that $c_P \simeq 5092, 3589, 3386$ m/s for these materials, respectively, so that $\dot{a}_0$ is lower than c_P by more than one order of magnitude. Neglecting compressibility provides, with $B_2 = 2$, values of $\dot{a}_0$ lower than the above ones by a relative error of about 5×10^{-3}. Though it is strictly valid for a constant applied stress (since $\dot{a} = \text{const.}$ by hypothesis), Eqn. (B.18) nonetheless provides the leading-order behavior for a time-varying stress, which is the type of loading considered in Sec. 2.2 where use is made of this equation. In practice, transient corrections mainly consist in damped oscillations around this leading behavior, as was checked by finite-element calculations, and are neglected in this work.

In the incompressible limit (where $c_L = c_P = \infty$) Eqn. (B.14) reduces to $\dot{a} = [Y/(2\mu)]^{1/3}\dot{c}$ (this relation is encapsulated in the equations of Carroll and Holt (1972) in the limit of vanishing initial porosity). Hence in general, it is expected that $\dot{a} \ll \dot{c} \leq c_P$. Combined with the above low-velocity solution, this suggests the following approximation to (B.14)

$$\alpha_P^3 = \beta\,\gamma_P^3/(1 - \gamma_P^2), \tag{B.19}$$

which contains in particular the incompressible limit (where $\gamma_P \to 0$). This approximation, which preserves (B.17) up to the neglected terms, and which can be solved analytically for γ_P, proves useful to compute numerically the stress in numerical implementations of the model.

Figure B.1 compares Eqn. (B.14) with either stress- or velocity-driven finite-element numerical results. These data points are reasonably well reproduced by the solution of Eqn. (B.14), in spite of the underlying approximations. The solution to Eqn. (B.19) is indistinguishable to the eye from the latter. Also shown are the linear approximation (B.16) and the above incompressible (linear) solution.

---

[4] However, their expression, written in terms of μ and Y, is that of the incompressible case.

It should be noted that the incompressible limiting value $B_2 = 2$ markedly differs from the value $B_2 = 3/2$ which one easily deduces from Carroll and Holt's (1972) incompressible calculation in the limit of zero initial porosity, where convection is accounted for. Though a detailed study of the influence of convective terms in the compressible case lies beyond the scope of this paper, this difference indicates that convection may be important in accurately determining the coefficient $\dot{a}_0$ in (B.18), the difference between the approaches concerning a numerical coefficient of order one. Taking $B_2 = 3/2$ instead of 2, Eqn. (B.17) is compatible with the work of Molinari and Wright (2005) in the limit of stationary growth of incompressible materials, and close to the result given by Tonks et al. (2002). Thus, the obtained cavitation threshold, and the general form of this law hold in any case, which is a sufficient conclusion for the present purpose.

C   Inhibition probability

To define the probability that a point $\mathbf{x}$ at a time t be relaxed, it is preferable to invert the problem by looking into the past of the considered site to know if a cavity is able to inhibit its nucleation (this method, first proposed by Cahn (1996), was found independently by two of the present authors (Denoual et al. 1997; Denoual, 1998). Two zones are distinguished. First, a zone in which the nucleated cavities never inhibit the considered site (see dashed part of Fig. 5(b) when $\tau < t$). In the second (complementary) zone, any nucleated cavity will inhibit $\mathbf{x}$. This zone is referred to as the *horizon* (Cahn, 1996; Denoual et al. 1997; Denoual, 1998).

The inhibition probability $P_{\text{inh}}(t)$ is written as the product of the elementary probabilities $\Delta P_{\nexists}(\tau)$

$$1 - P_{\text{inh}}(t) = \prod_{\tau=0}^{t} \Delta P_{\nexists}(\tau) \tag{C.1}$$

where $\Delta P_{\nexists}(\tau)$ is the probability of finding no new sites during a time increment $\Delta\tau$ in a zone $V_{\text{inh}}(t - \tau)$. It suffices to apply Eqn. (1) with $V = V_{\text{inh}}(t - \tau)$ for an intensity $\frac{dn_{\text{tot}}}{d\tau}[\sigma(\tau)]\,\Delta\tau$, since it still is a Poisson process

$$\Delta P_{\nexists}(\tau) = \exp\left[-\frac{\mathrm{d}n_{\text{tot}}}{\mathrm{d}\tau}[\sigma(\tau)]\,\Delta\tau\, V_{\text{inh}}(t - \tau)\right]. \tag{C.2}$$

The probability $P_{\text{inh}}(t)$ becomes

$$1 - P_{\text{inh}}(t) = \exp\left[-\sum_{\tau=0}^{t}\frac{\mathrm{d}n_{\text{tot}}}{\mathrm{d}\tau}[\sigma(\tau)]\,\Delta\tau\, V_{\text{inh}}(t - \tau)\right]. \tag{C.3}$$

In the continuous limit $\Delta\tau \to 0$, rewriting the sum as an integral eventually yields Eqs. (11) and (12).